Materials Today Bio 31 (2025) 101568

Contents lists available at ScienceDirect

Materials Today Bio

journal homepage: www.journals.elsevier.com/materials-today-bio

Intranasal delivery of AEP inhibitor-loaded neuron-targeted liposome ameliorates radiation-induced brain injury

Keman Liao [a,b,c,1], Yan Gao [d,e,1], Mengdan Cheng [d,e,1], Yibing Zhang [a,b,c,1], Jianyi Zhao [a,b,c], Li Zhou [a,b,c], Ran Wu [a,b,c], Gang Cai [a,b,c,****], Lu Cao [a,b,c,***], Jiayi Chen [a,b,c,**], Yingying Lin [a,b,c,*]

[a] Department of Radiation Oncology, Ruijin Hospital, Shanghai Jiaotong University School of Medicine, Shanghai, 200025, China
[b] Shanghai Key Laboratory of Proton-Therapy, Shanghai, 201801, China
[c] Institute for Medical Imaging Technology, Shanghai, 201800, China
[d] Department of Neurosurgery, Jiangnan University Medical Center, 214000, China
[e] Wuxi neurosurgical Institute, Jiangsu, 214000, China

ARTICLE INFO

Keywords:
Asparagine endopeptidase
Radiation-induced brain injury
Nose-to-brain
Liposomes

ABSTRACT

Acute exposure to high-dose radiation during head and neck tumors radiotherapy can result in radiation-induced brain injury (RIBI), characterized by neurocognitive deficits, dementia, and epilepsy. Asparagine endopeptidase (AEP), a cysteine proteinase, is effective in preventing neurodegenerative diseases and RIBI. However, the limited permeability of selective AEP inhibitor (AEPI) delivery to the brain reduces its effectiveness in preventing RIBI. This study constructed a nose-to-brain delivery platform for AEPI by encapsulating it in liposomes that are surface modified with rabies virus glycoprotein (RVG29), creating RVG29-AEPI liposomes. These RVG29-AEPI liposomes demonstrated efficient cellular uptake and blood-brain barrier penetration *in vitro* and *in vivo*. RVG29-AEPI liposomes effectively shielded DNA from radiation-induced damage and resulted in more effective reactive oxygen species removal than liposomes in primary neurons and microglial cells. Notably, the treatment with RVG29-AEPI liposomes (10 mg/kg AEPI) was highly systemically safe and significantly reduced brain injury. Behavioral tests demonstrated that RVG29-AEPI liposomes-treated mice had less radiation-induced brain damage and motor dysfunction. Moreover, it significantly prevented neuronal injury and microglia cell activation under photon and modern proton irradiation. These findings demonstrate the potential of nose-to-brain medication delivery of RVG29-AEPI liposomes for effective radioprotection, indicating a viable technique with enormous potential for clinical translation.

1. Introduction

Radiation therapy is a typical effective non-surgical treatment for primary brain tumors and their metastases; however, large doses of ionizing radiation cause radiation-induced brain damage (RIBI) [1]. Brain cells produce DNA damage and reactive oxygen species (ROS), resulting in inflammatory responses that damage neurons and severely injures adjacent cells upon irradiation [2]. These biochemical

---

* Corresponding authors. Department of Radiation Oncology, Ruijin Hospital, Shanghai Jiaotong University School of Medicine. Shanghai 200127, China. Shanghai Key Laboratory of Proton-Therapy, Shanghai 201801, China. Institute for Medical Imaging Technology, Shanghai, 201800, China.

** Corresponding author. Department of Radiation Oncology, Ruijin Hospital, Shanghai Jiaotong University School of Medicine. Shanghai 200127, China. Shanghai Key Laboratory of Proton-Therapy, Shanghai 201801, China. Institute for Medical Imaging Technology, Shanghai, 201800, China.

*** Corresponding authors. Department of Radiation Oncology, Ruijin Hospital, Shanghai Jiaotong University School of Medicine. Shanghai 200127, China. Shanghai Key Laboratory of Proton-Therapy, Shanghai 201801, China. Institute for Medical Imaging Technology, Shanghai, 201800, China.

**** Corresponding author. Department of Radiation Oncology, Ruijin Hospital, Shanghai Jiaotong University School of Medicine, Shanghai 200127, China. Shanghai Key Laboratory of Proton-Therapy, Shanghai 201801, China. Institute for Medical Imaging Technology, Shanghai, 201800, China.

E-mail addresses: cg11855@rjh.com.cn (G. Cai), cl11879@rjh.com.cn (L. Cao), cjy11756@rjh.com.cn (J. Chen), yylin@sibs.ac.cn (Y. Lin).

[1] These authors contributed equally to this work.

https://doi.org/10.1016/j.mtbio.2025.101568
Received 3 October 2024; Received in revised form 31 December 2024; Accepted 8 February 2025

alterations can cause acute, early, or late-delayed symptoms [3]. Significant progress has recently been made in treating RIBI, particularly in blood-brain barrier repair and immune regulation. Several drugs, such as corticosteroids and bevacizumab, are used as first-line treatments for RIBI. In addition, clinical trials have assessed the role of pharmaceuticals, such as apatinib [4] and thalidomide [5], in ameliorating the side effects of brain irradiation. Additionally, biological therapies, such as PARP inhibitors [6], stem cell therapy [7], or nasal delivery of antagomiR-122 [8], are being actively used as potential strategies against RIBI. However, the efficacy and long-term safety of these treatments still require further investigation. In addition to the underlying complex pathogenic mechanisms, this mode of delivery causes minimal blood-brain barrier (BBB) penetration. Hence, it is critical to devise an effective strategy to simultaneously address these issues.

A potential target for RIBI is asparagine endopeptidase (AEP), a cysteine proteinase belonging to the C13 family of peptidases [8]. AEP levels are elevated and activated under damaged or degenerative conditions, such as Alzheimer's disease [9,10]. Tau and the amyloid precursor protein (APP), the primary components of Alzheimer's disease, are cleaved by active AEP. APP is cleaved by AEP at N373 and N585, whereas tau is cleaved at N255 and N368 [11]. Additionally, our previous research demonstrated that AEP is highly expressed in various solid tumors and is associated with poor prognosis by cleaving wildtype-p53, tropomodulin-3 (Tmod3), and DEAD-box helicase 3 X-linked (DDX3X) [12–14]. Furthermore, AEP plays a vital role in RIBI by targeting microglia to trigger neuronal senescence. Moreover, the enzymatic activity of AEP can be reduced by PPI drugs, such as esomeprazole and small-molecule inhibitors [8]. However, these drugs exhibit low levels of blood-brain barrier crossing. To efficiently prevent RIBI, AEPI delivery systems were created based on their pathophysiological activities.

Liposomes are vesicular structures composed of polysaccharides, sterols, and phospholipids arranged in bilayers through lipid interactions. Many modified liposomes have been used in numerous medications and the clinical studies as intriguing candidates [15]. Several innovative methods for improving systemic brain delivery have been developed using liposomes as carriers for treating brain-targeted diseases. One such method involves conjugating naturally occurring transporting ligands to facilitate transcytosis [16–18]. Rabies virus glycoprotein (RVG29), a 29-residue peptide derived from the RVG, has been shown to recognize neural nAchR or gamma-aminobutyric acid (GABA) receptor, and it can be administered intranasally and utilized as an effective "BBB shuttle" to promote brain uptake [19,20]. Therefore, proper surface modification of RVG2 liposomes could help develop optional therapies to inhibit RIBI progression.

This study presents a unique nose-to-brain delivery platform for AEPI to prevent RIBI. RVG29-AEPI liposomes are absorbed by primary neurons and microglial cells and served as an effective scavenger of ROS. The ability of RVG29-AEPI liposomes to adequately protect against brain injury in both standard and new forms of radiation *in vivo*, along with their behavioral tests are evaluated. These findings offer a thorough justification for the potential clinical application of RVG29-AEPI liposomes as brain radioprotectors in the future.

2. Materials and methods

2.1. Synthesis and characterization of RVG29-AEPI liposomes

RVG29-AEPI liposomes and RVG2-liposome were synthesized by Ruixi Biological Technology (Xi'an, China). Briefly, AEP inhibitor (MCE, HY-114174, USA) aqueous solution was added for hydration after soybean lecithin, cholesterol, DSPE-PEG2000-RVG29, and Cy5 (supplied by Ruixi Biological Technology) were all dissolved in 5 mL of chloroform. Subsequently, an aqueous solution of an AEP inhibitor (MCE, HY-114174, USA) was added for hydration, and the mixture was and evaporated into a film in a sample vial under reduced pressure. The mass ratio of soy lecithin: cholesterol: DSPE-PEG2000-RVG29: CY5 was 50:10:5:1. The samples were treated with a liposome extruder and ultrasonography (polycarbonate film, 200 nm pore size, Avanti Research, 610006, UK). After removing the unloaded AEP inhibitor using a nanodialysis device (polycarbonate membrane, pore size 30 nm, R-30120, Ruixi Biological Technology, China), 10 mL of deionized water was added.

Table 1
The size, polydispersity index (PDI) and zeta potential of RVG29-AEPI Liposomes.

	Hydrodynamic size (nm)	PDI	Zeta potential (mV)
First time	120.11	0.205	−23.40
Second time	11248 ± 672	0.213	−20.81
Third time	122.36	0.206	−21.43
Average value	120.5 ± 1.86	0.208 ± 0.005	−21.88 ± 1.52

The size, polydispersity index (PDI) and zeta potential of the liposomes were measured by a nanometer particle size potentiometer (NanoBrook 90plus PALS, Brookhaven, USA) for 10 min under 25 °C. These parameters are listed in Table 1. To evenly distribute the medication particles, an ultrasonic device (JP-020, Jiemeng Technology, China) was used for 30 s at 40 kHZ and 180 W. The encapsulation efficiency was determined using a methodology described by Chen et al. After 48 h, the release curve of the RVG29-AEPI liposomes was evaluated in 1 × PBS (PH 7.4; Servicebio, G4202, China). The intensity of the fluorescence of RVG29-AEPI liposomes and their transmission electron microscopy (TEM) images were obtained.

The liposomal samples were diluted to 0.5 mg/mL w/v in RNAse/DNAse free water, loaded on to charged copper grids for adsorption, and a 1 % solution was prepared with phosphoric acid buffer and washed twice in distilled water to remove the excess stain. Subsequently, it was left to dry. The samples were examined by the TEM studies using a Morgagni transmission electron microscope (FEI Instruments, Hillsboro, OR, USA).

2.2. Primary cell culture and reagents

Primary neurons and microglial cells were dissected from newborn mice and the detailed steps are listed in the Supplementary Materials.

The American Type Culture Collection (ATCC) provided the BV2 cell lines, which were then cultured in Dulbecco's modified Eagle's medium (DMEM) media (TBD, 10569) with 10 % fetal bovine serum (FBS) (Gibco, 10270-106) and 100 IU/ml penicillin/streptomycin (Gibco) at 37 °C in a humidified incubator with 5 % CO2.

2.3. Cellular uptake of liposomes

Liposomes (equivalent to 23.4 μg/mL AEPI) were applied to primary neurons and primary microglial cells and incubated for 1 or 2 h at 37 °C. The cells were then rinsed twice with cold PBS (Servicebio, G4202, China) and fixed in 4 % paraformaldehyde (Servicebio, G4202, China). To determine the amount of DNA, the nuclei were stained with 4′,6-diamidino-2-phenylindole (DAPI). Images of the labeled cells were captured using a fluorescence microscope (Leica DM4B, Germany).

2.4. Frozen section preparation and immunofluorescence staining

The tissues were immersed in a compound with an ideal cutting temperature for a specific period after irradiation and quickly frozen for sectioning. Using a cryostat, sections with thicknesses of 20 μm/25 μm were cut and placed on glass slides.

For immunofluorescence labeling, the following primary antibodies were used: anti-GFAP (1:500, Invitrogen, 130300), anti-NeuN (1:200, Abcam, ab104224), anti-γ-H2A.X (1:200) (ab26350; Abcam), ROS probe (1:1000, Jiancheng Biotech, S0033S), and anti-IBA1 (1:500, Abcam, ab178846). The corresponding primary and secondary antibodies were goat anti-rabbit IgG-AF488 antibody (1:500, Absin, Abs20025), goat anti-mouse IgG-AF488 antibody (1:500, Absin, Abs20013), goat anti-mouse IgG-AF594 antibody (1:500, Absin, Abs20146), goat anti-rabbit IgG-AF594 antibody (1:500, Absin, abs20145), and goat anti-rat IgG (H + L) -Plus 594 (1:500, Thermo, A48264). To visualize the nuclei, the slices were washed with PBS and counterstained with DAPI. The slides were then examined using a Leica DM4B fluorescence microscope (Germany).

2.5. *Clonogenic assay*

The BV2 cells were seeded in culture dishes at an appropriate density and cultured in DMEM supplemented with 10 % FBS. After 24 h, the cells were treated with AEPI-RVG-liposomes (corresponding to 23.4 μg/mL AEPI) or liposomes for 1 h. Subsequently, the cells were irradiated by X-rays (5 Gy). The medium was then changed every three days until cell clones (each clone contained more than 50 cells) were formed. The cell clones were washed thrice with PBS (Servicebio, G4202, China), fixed with 4 % paraformaldehyde (Servicebio, G4202, China) for 15 min, and visualized by staining with crystal violet (Beyotime, Shanghai, China).

2.6. *Animals and biosafety test*

Male C57BL/6 mice, aged 7–8 weeks, were used in this study (LINGCHANG BIOTECH, Shanghai, China). The standard parameters were 25 °C, 55–60 % humidity, and a 12-h light/dark cycle. All experimental procedures were conducted in accordance with the Guide for the Care and Use of Laboratory Animals and were approved by the Animal Research Ethical Council at Ruijin Hospital, Shanghai Jiaotong

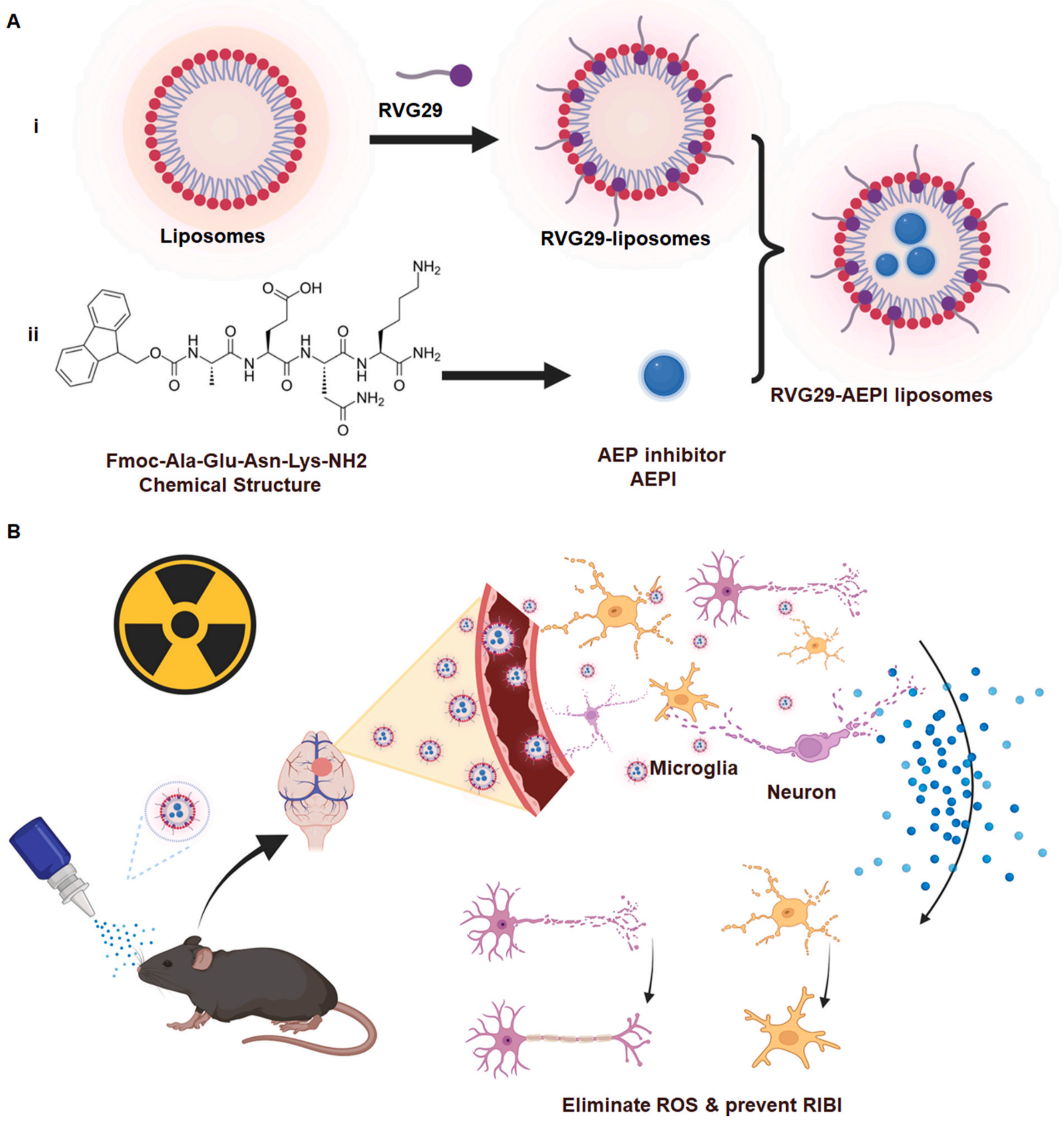

Fig. 1. A schematic representation of the liposomes used in targeted RIBI prophylaxis. (A) The synthetic process of making RVG29-AEPI liposomes: (i) Encapsulated RVG29 in liposomes. (ii) The structure of AEP inhibitor. (B) Intranasal delivery of RVG29-AEPI liposomes prevents RIBI, releases AEPI, removes ROS, and crosses the blood-brain barrier.

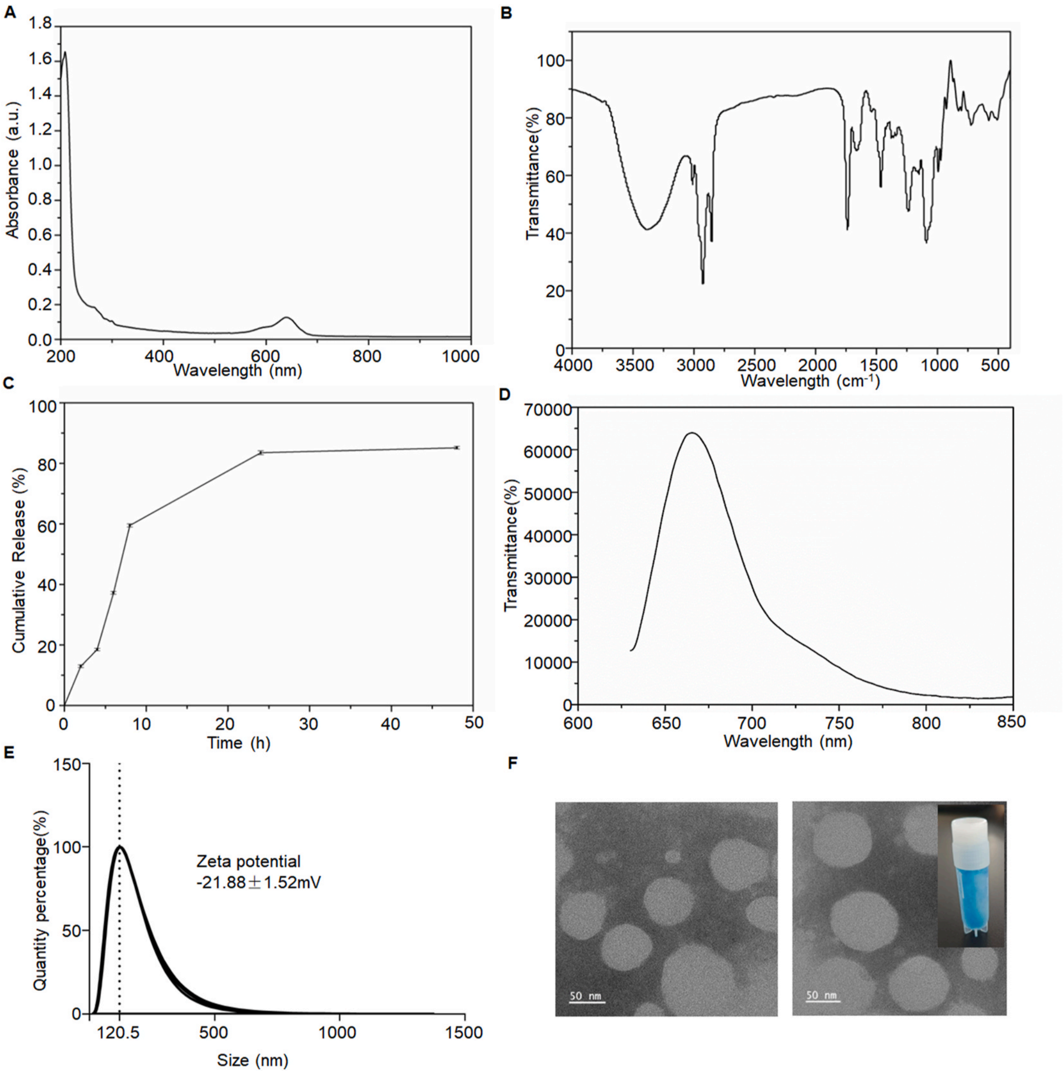

Fig. 2. RVG29-AEPI Liposome Characterization. (A) The UV–visible absorption spectra of RVG29-AEPI liposomes. (B) The infrared transmission spectra of RVG29-AEPI liposomes. (C) The release curve of RVG29-AEPI in 1 × PBS (pH 7.4) for a 48-h period. (D) The RVG29-AEPI Liposomes' fluorescence intensity. (E) The effective diameter distribution and ζ-potential distribution of RVG29-AEPI liposomes. (F) The TEM image of RVG29-AEPI Liposomes, with the scale bar representing 50 nm.

University School of Medicine. An animal atomized drug delivery apparatus (ZL-005; Anhui Yaokun Biotechnology Co., Ltd. China) was used to administer the liposome powder. The device used compressed air to produce negative pressure to suck up the liquid medicine and then atomized the liquid medicine into a very fine mist to spray it out. This device allowed the mice to inhale the drug. Before administration, the reservoir of an insufflator was filled with liposomes (corresponding to AEPI 10 mg/kg) and accurately weighed, and the device was assembled according to the manufacturer's instructions. Each loaded device was weighed before and after actuation to determine the quantity of the administered powder. The gas flow rate was set at 1 L/min, and the duration of administration was approximately 20 s. The AEPI group was administered a dose of 10 mg/kg via the nasal route.

The heads were removed and fixed in 4 % paraformaldehyde after 2 h administration, then decalcified and dehydrated. The transverse plane from the top of the head to jaw were sectioned, stained. The slides were then examined by confocal (Leica SP8, Germany).

Eight male C57BL/6 mice were fed PBS or RVG29-AEPI liposomes, equivalent to 10 mg/kg AEPI, daily for 14 days as part of an *in vivo* biosafety test. The mice were euthanized after 14 days, and hematological and blood chemistry analyses were performed on whole blood samples. The primary organs were stained with hematoxylin and eosin (H&E).

2.7. Irradiation

Irradiation treatments were performed at the Shanghai Key Laboratory of Proton Therapy. For photon therapy, whole-brain photon irradiation was performed on five mice using a 6-MV X-ray beam at a dose of 10 Gy/1 Fx and dose rate of 300 cGy/min. The source-surface distance (SSD) was set to 100 cm with 0.5 cm of solid water for dose building, and a radiation field of 30 × 2.5 cm was used. The irradiation was conducted using a medical linear accelerator (Varian Trilogy, FL, USA). For proton therapy, proton pencil-beam scanning was performed at a fixed horizontal proton beam line. A dose of 10 Gy (RBE) was administered to the animals. A 30 × 2 cm irradiation field was utilized, with a 70.6–112.5 MeV pencil beam scanning the spread-out Bragg peak (SOBP) using a RayStation treatment planning system. The pencil beam-scanned SOBP had a range of 10 cm and plateau width of 5 cm, delivering the prescribed dose of 10 Gy, calculated using the Monte Carlo approach.

2.8. LC-MS/MS method for AEPI Quantification in biological samples

LC-MS/MS experiments were performed with an ACQUITY UPLC

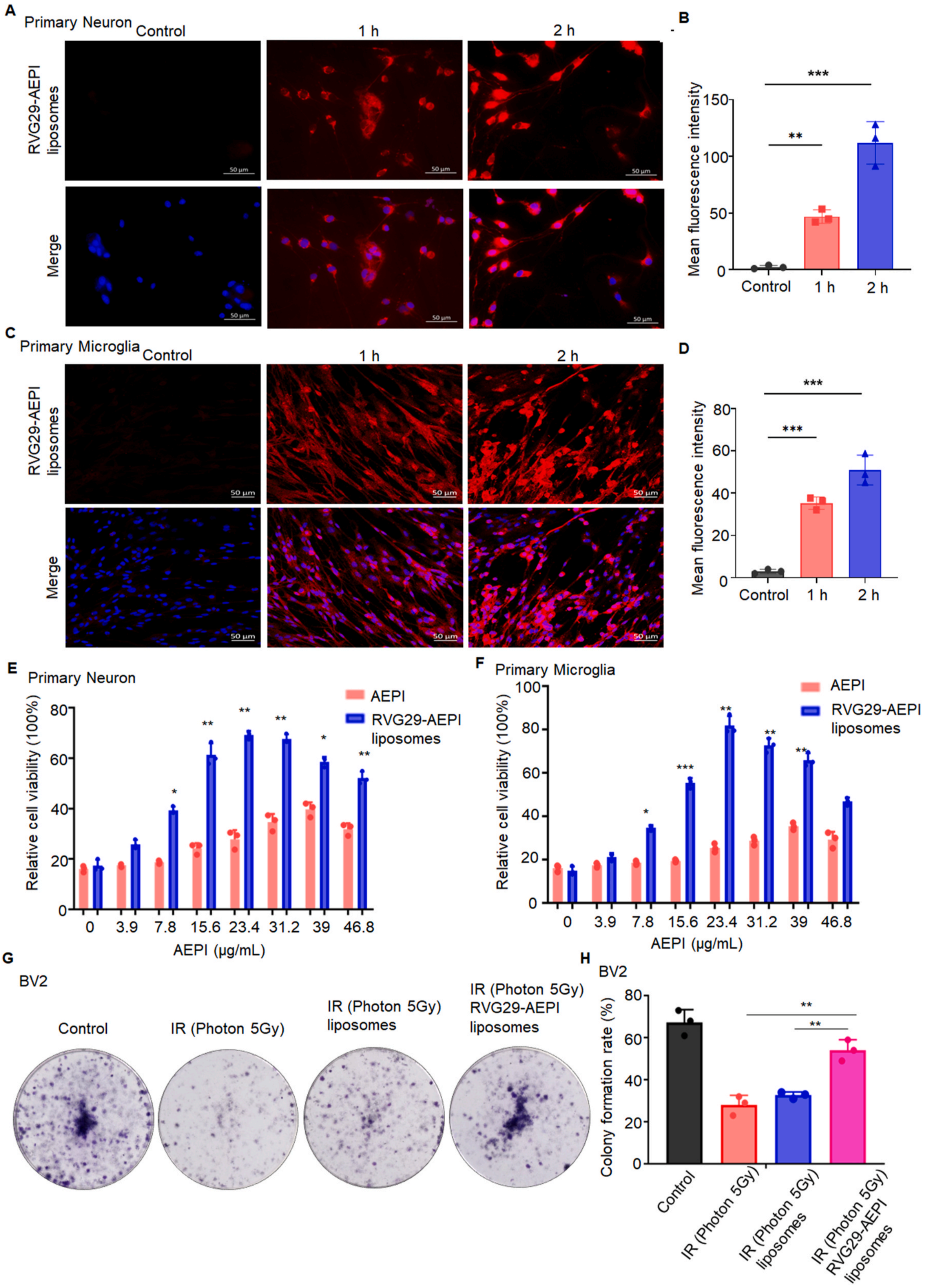

Fig. 3. RVG29-AEPI Liposomes outperformed AEPI in terms of cellular absorption, reduced toxicity, and enhanced protection of brain cells under photon therapy. (A) The cellular uptake of RVG29-AEPI liposomes by primary neurons. Scale bar: 50 μm. (B) The average fluorescence intensity after being incubated for 1 or 2 h ($n = 3$) with RVG29-AEPI liposomes. (C) The cellular uptake of RVG29-AEPI liposomes by primary microglial cells. Scale bar: 50 μm. (D) Average fluorescence intensity after being incubated for 1 or 2 h ($n = 3$) with RVG29-AEPI liposomes. (E, F) Cytotoxicity of drug mixtures and RVG29-AEPI liposomes in primary neurons (E) and primary microglial cells (F) ($n = 3$). (G, H) BV2 colonies exposed to 5 Gy irradiation of different groups (Control, IR, IR + liposomes, IR + RVG29-AEPI liposomes). The data are shown as the mean ± standard deviation (s.d.) from three separate studies. ***: $p < 0.001$. **: $p < 0.01$. *: $p < 0.05$.

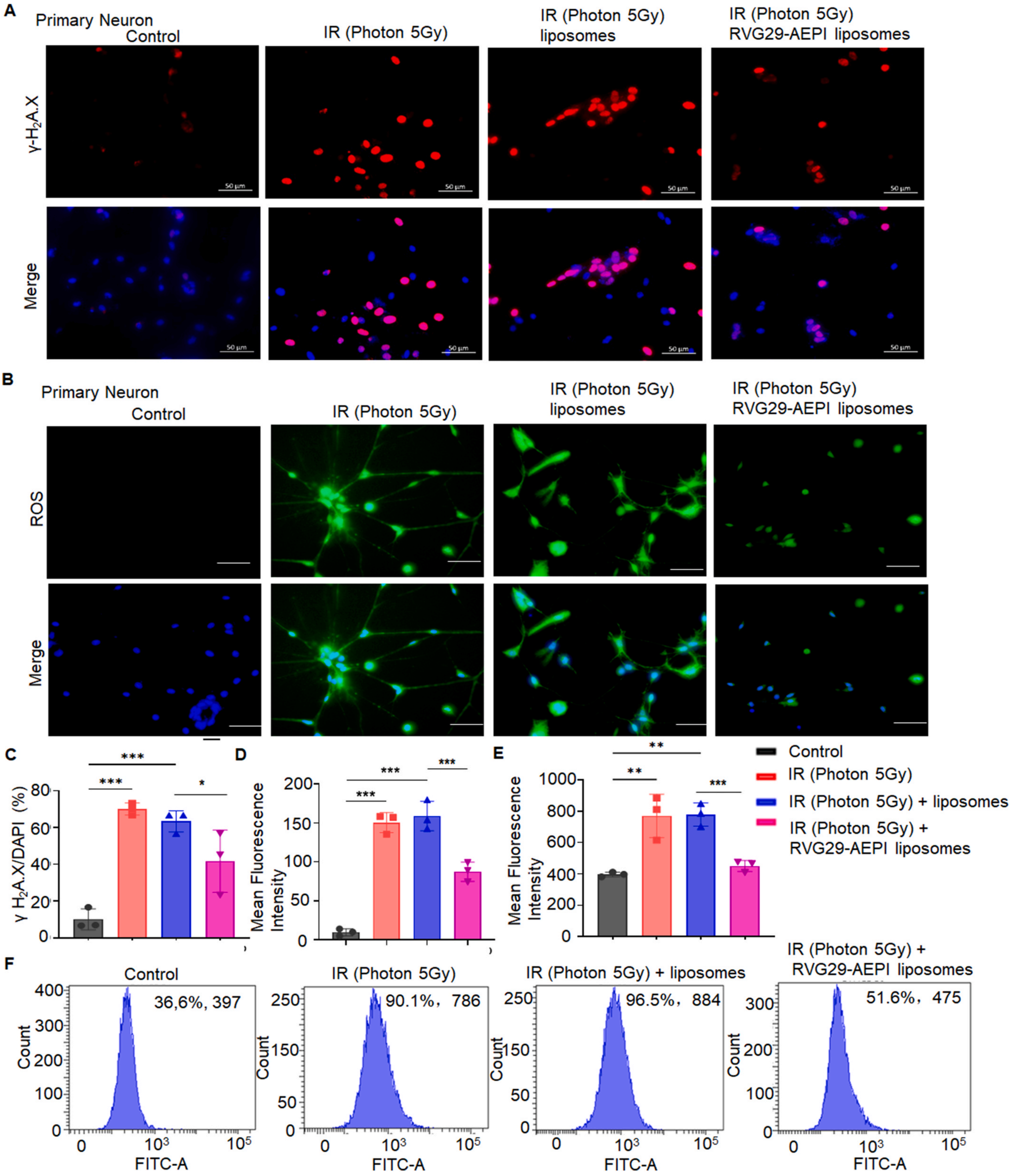

Fig. 4. RVG29-AEPI Liposomes could efficiently scavenge ROS and protect DNA from damage in primary neurons under photon therapy. (A, C) γ-H_2A.X immunofluorescence staining of primary neurons following various treatments (red signal). Scale bar: 50 μm. (B, D) Fluorescence images for detecting ROS produced by primary neurons following various treatments. Scale bar: 50 μm. (E, F) Flow cytometric profiles showing the production of intracellular ROS in primary neurons following various treatments. The three separate experiments' means ± standard deviations are used to illustrate the data. ***: $p < 0.001$. **: $p < 0.01$. *: $p < 0.05$.

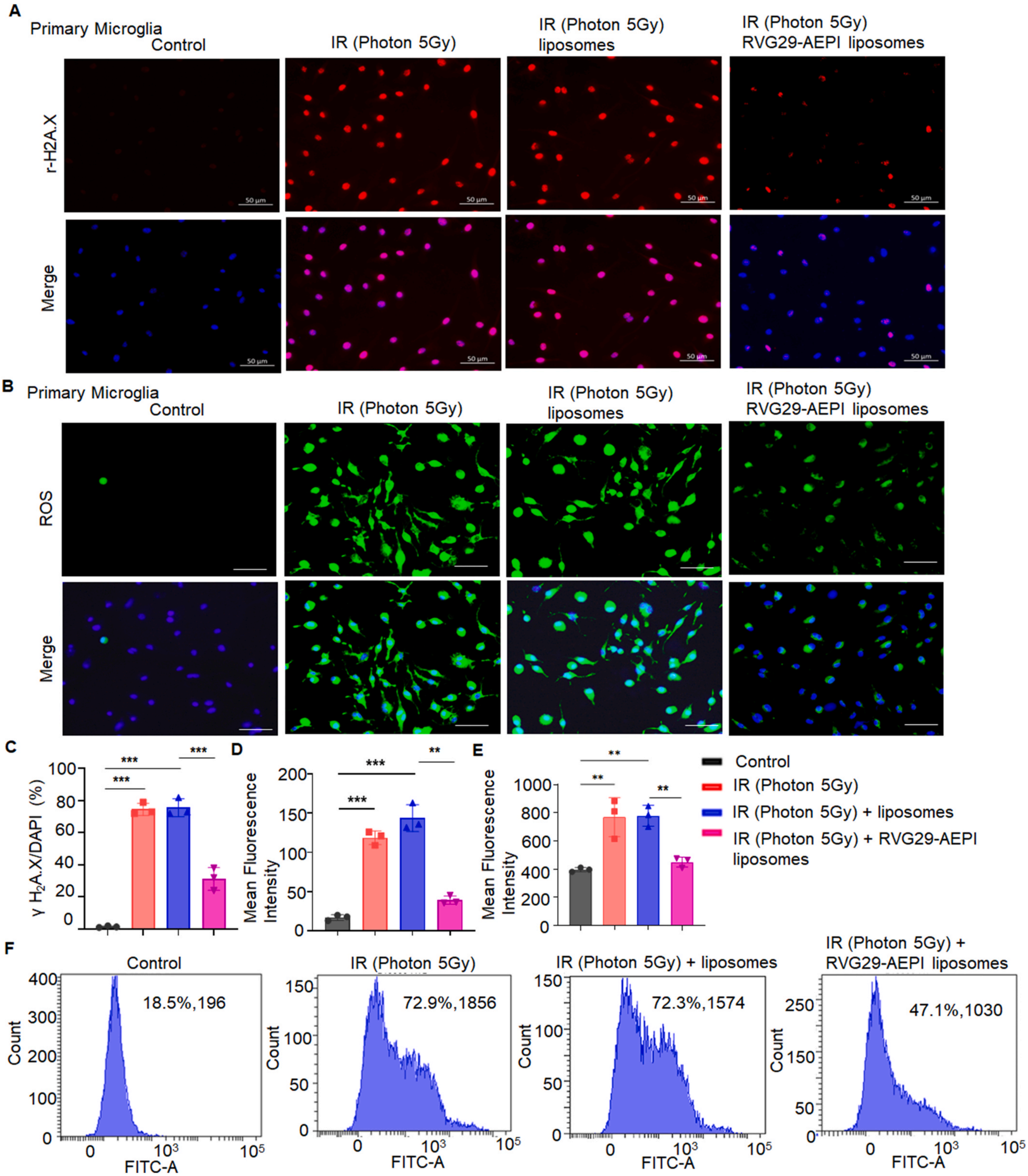

Fig. 5. RVG29-AEPI Liposomes could efficiently scavenge ROS and protect DNA from damage in primary microglial cells under photon therapy. (A, C) γ-H_2A.X immunofluorescence staining of primary microglial cells following various treatments (red signal). Scale bar: 50 μm. (B, D) Fluorescence images for detecting ROS produced by primary microglial cells following various treatments. Scale bar: 50 μm. (E, F) Flow cytometric profiles showing the formation of intracellular ROS in primary microglial cells following various treatments. The three separate experiments' means ± standard deviations are used to illustrate the data. ***: $p < 0.001$. **: $p < 0.01$.

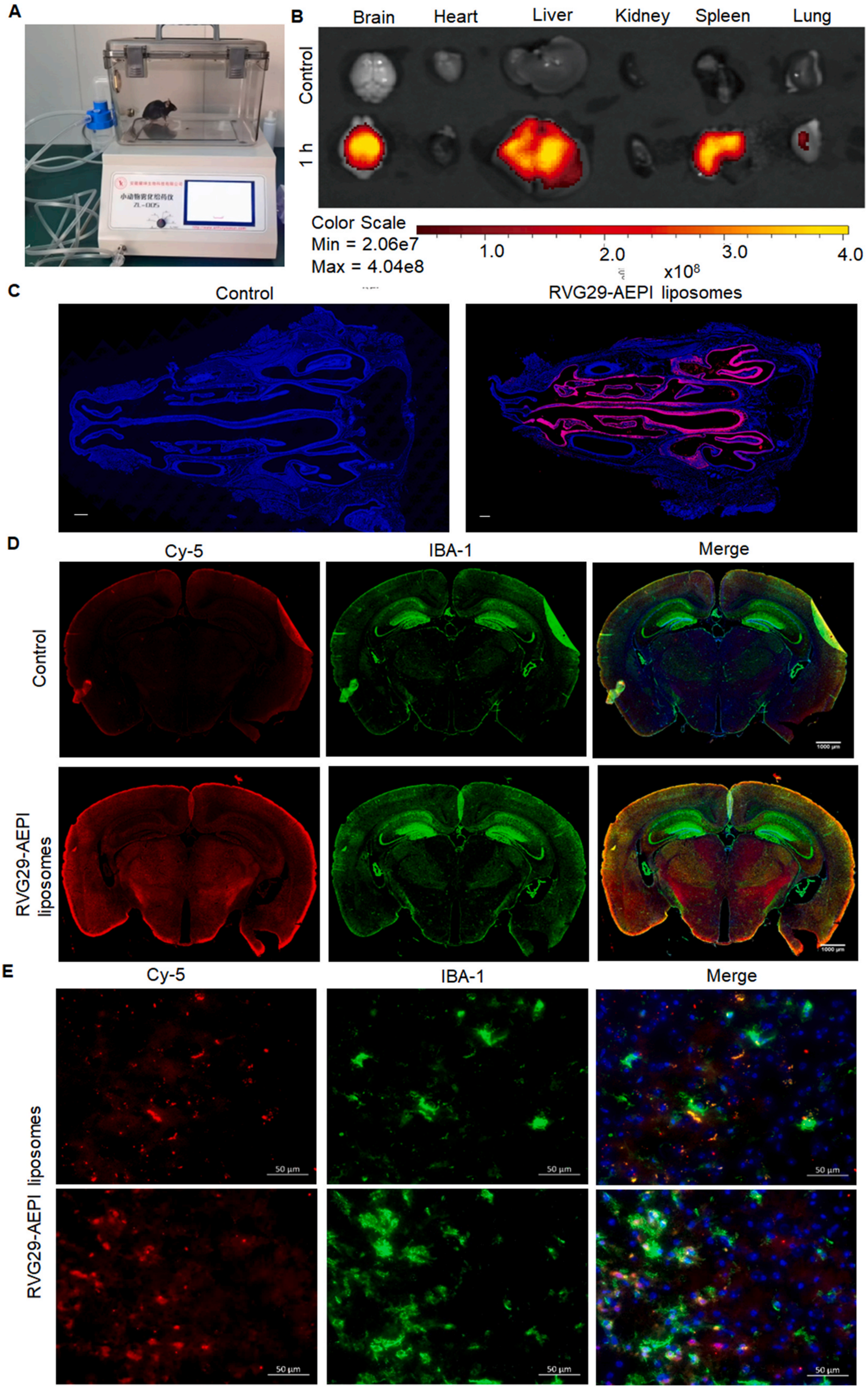

Fig. 6. Brain cells absorbed RVG29-AEPI liposomes *in vivo*. (A) The atomizing machine used in this experiment. (B) In vivo Imaging System (IVIS) images of major organ from mice captured at 1 h after nasal delivery of RVG29-AEPI liposomes and PBS. (C) The distribution of RVG29-AEPI Liposomes in olfactory mucosa. Scale bar: 500 μm. (D) The representative fluorescence images of RVG29-AEPI liposomes Cy5-labeled and IBA1 in mouse brain slices. Scale bar: 1000 μm. (E) Colocalization of RVG29-AEPI liposomes and IBA1 (orange signal) in mouse brain slices. Scale bar: 50 μm.

BEH C18 (100 × 2.1 mm, 1.7 μm) system working at 35 °C. Mobile phase A was H2O with 0.1 % formic acid, and mobile phase B was a 0.1 % formic acid–acetonitrile solution. The flow rate was 0.3 mL/min. Mass spectrometry (AB Sciex Qtrap 6500+) was performed using an electron spray ionization (ESI) source in the positive ion scan, and the multiple reaction monitoring (MRM) mode was used to detect the target object. The target MRM ion pairs were 682.5 → 179.2 and 682.5 → 226.1, and the corresponding de-clustering voltages (DP) and collision energies (CE) of each ion pair were 81.35/89.22 V (DP) and 48.38/43.11 V (CE), respectively. The parameters of each ion source in this method were as follows: curtain gas, 35.0 psi, collision gas, medium; and spray voltage, 5000 V. The temperature was set to 450 °C, auxiliary heating gas (Gases 1 and 2) was 50 psi, and the dwell time was 120 ms.

More detailed steps are presented in the Supplementary Materials.

2.9. H&E staining

After deparaffinization and hydration, the paraffin-embedded slices were stained with hematoxylin for 5 min to perform H&E staining. Subsequently, they were briefly treated with 1 % hydrochloric acid alcohol, and they rapidly turned blue when exposed to 0.6 % ammonia. The water was allowed to run gently. The slices were stained for 3 min in an eosin dye solution. Neutral resin was used to seal the area after dehydration, and a panoramic scanner was used to capture pictures (Pannoramic DESK, P-MIDI, 3D HISTECH, Hungary).

2.10. Behavior tests

2.10.1. Open field

A wide field was utilized to investigate activities and assess anxiety levels. A typical open field (a 100 × 100 cm^2 square arena with 70 cm high walls) served as the test configuration. Each rat was trained for 5 min. The animal in the box was tracked, and the distance traveled was measured to assess its exploratory activities.

2.10.2. Rotarod tests

Rotarod tests were performed as previously described [8]. The mice were placed on a spinning drum, and the speed was gradually increased from 4 to 40 rpm over 5 min. The time required for the mice to slip off the drum was recorded.

2.11. Statistics

Data were analyzed using SPSS 21.0 (International Business Machines Corporation, Armonk, NY, USA). Two-tailed Student's t-tests, one-way ANOVAs, Pearson correlation analyses, Kaplan–Meier analyses, and log-rank tests were performed. The statistical P value was set to less than 0.05. GraphPad Prism 7 (GraphPad Software Inc., San Diego, CA, USA) was used to construct the statistical graphs.

3. Results

3.1. Synthesis and characterization of RVG29-AEPI liposomes

RVG29-AEPI liposomes were successfully generated by encapsulating AEPI into RVG29-liposomes (Fig. 1A). The RVG29-AEPI liposomes can scavenge oxygen-derived free radicals and prevent DNA damage when administered intranasally via the olfactory nerve (Fig. 1B).

Next, we measured the absorption spectra, *in vitro* release, encapsulation rate, particle size, and zeta potential of the RVG29-AEPI liposomes. The RVG29-AEPI liposomes exhibited distinct absorption peaks at 200 and 800 nm (Fig. 2A). The liposomes also showed a distinctive broad peak attributable to hydroxyl stretching vibrations near 3500 cm^{-1} and multiple characteristic absorption peaks in the 1500-1000 cm^{-1} range in infrared transmission spectra (Fig. 2B). The cumulative release curve of RVG29-AEPI liposomes is shown *in vitro*. Drug release was relatively active in the first 30 h, and then stabilized until 48 h (Fig. 2C). The RVG29-AEPI liposomes showed 78 % encapsulation efficiency and 7.8 % loading efficiency, also the drug/lipid ratio was 1:10. Furthermore, they strongly emitted light at an excitation wavelength of 680 nm (Fig. 2D). The RVG29-AEPI liposomes had a hydrodynamic diameter of 120.5 ± 1.86 nm and PDI of 0.208 ± 0.005, according to NTA measurements (Fig. 2E). Fig. 2E shows that the negative ζ-potential of −21.88 ± 1.52 mV provides good shelf stability due to interparticle charge repulsion. The RVG29-AEPI liposomes had a consistent spherical shape and a size of approximately 50 nm, as determined by TEM (Fig. 2F). These findings demonstrated the effective encapsulation of AEPI on RVG29-Liposomes.

3.2. RVG29-AEPI liposomes showed efficient neural cellular uptake and effective protection on primary cells in vitro

To confirm the effect of RVG29-AEPI liposomes *in vitro*, the neural cellular uptake was initially measured. Primary neurons and microglial cells were used to assess the cellular absorption of the RVG29-AEPI liposomes tagged with Cy5. The cells were treated with RVG29-AEPI at 37 °C for 1 or 2 h. Fluorescence imaging showed that RVG29-AEPI liposomes had high cellular uptake in both primary neurons (Fig. 3A and B) and primary microglial cells (Fig. 3C and D). The cytotoxicity of RVG29-AEPI liposomes on both cell lines was found to be lower than that of free AEPI within the concentration range 7.8–46.8 μg/mL under irradiation (Fig. 3E and F). Colony formation assays also demonstrated that RVG29-AEPI liposomes provided superior protection to irradiated BV2 cells than IR and IR + liopsomes (Fig. 3G and H).

According to the findings of the hemolytic toxicity test of the RVG29-AEPI liposomes, the proportion of hemolysis increased in tandem with the blood's AEPI content, which ranged from 15.6 to 109.2 μg/mL. A minor trend toward hemolysis was seen in 93.6 μg/mL RVG29-AEPI liposomes (3.52 ± 0.22 %). All the hemolysis rates were< 5 %. This concentration restriction was maintained for all subsequent *in vivo* experiments (Fig. S1).

The double-stranded DNA damage was investigated using γ-H_2A.X, an immunofluorescent marker of breakage. The results indicated clearly detectable γ-H_2A.X immunofluorescence in the IR group. Furthermore, treating primary neurons and microglia with RVG29-AEPI liposomes significantly reduced the red fluorescence signals of irradiated cells in the IR and IR + liposome groups. These results indicated that RVG29-AEPI-liposome could more effectively shield DNA from radiation-induced damage than liposomes (Fig. 4A, C, 5A, and 5C).

ROS production causes double-stranded DNA damage owing to interaction with DNA and inhibition of the rebuilding of broken double-stranded DNA [23]. Next, labeling and flow cytometry were used to explore the effect of AEP intervention on ROS scavenging in primary cells. Figs. 4B and 5B showed that IR and IR + liposomes produced clear green fluorescence signals, indicating substantial levels of ROS production. The RVG29-AEPI liposomes demonstrated more effective ROS removal than IR and IR + liposomes (Fig. 4D and 5D). Furthermore, a flow cytometric analysis revealed a similar trend (Fig. 4E, F, 5E, and 5F). These findings suggest that AEPI-loaded RVG2-targeted liposomes can be successfully absorbed by normal brain cells, thereby reducing irradiation-induced damage.

3.3. In vivo nasal delivery of RVG29-AEPI liposomes showed good penetration across an Intact BBB

The RVG29 was modified to allow partial penetration of the BBB. To determine whether liposomes can be transported to the brain via the intranasal route, their distribution in the brain was tracked, and their therapeutic efficacy *in vivo* was evaluated. An hour after nasal delivery (Fig. 6A), the mice were sacrificed, and their primary organs (heart, brain, liver, spleen, lungs, and kidneys) were positioned for *in vivo* imaging (Fig. 6B). As shown in Fig. 6B, RVG29-AEPI liposomes were most

Table 2
Mean brain tissue and serum levels of APEI following intranasal administration at 10 mg/kg. (n = 3 for each time interval).

	RVG29-AEPI liposomes (1-hr post administration)	AEPI (1-hr post administration)	Brain/Serum ratio
Brain (ng/g)	1334 ± 31.92	48.76 ± 33.02	0.12 ± 0.0475 (RVG29-AEPI liposomes)
Serum (ng/mL)	11248 ± 672	2733 ± 1675	0.018 ± 0.02 (AEPI)

abundant in the brain, liver and spleen, whereas they were less prevalent in the lungs, kidneys, and heart.

Subsequently, the distribution of RVG29-AEPI liposomes on olfactory mucosa was observed by panoramic confocal scanning (Fig. 6C). More liposomes adhered to olfactory mucosa in groups RVG29-AEPI liposomes. To determine the intracranial distribution of liposomes, the brains were dissected and sectioned. When Cy5-labeled liposomes were administered intranasally to mice, these particles were distributed throughout the olfactory bulb (OB) and cerebrum (CB) (Fig. 6D). The Cy5-labeled liposomes were distributed throughout the IBA1(+) cells, indicating that the liposomes could be delivered into the microglial cells in the brain (Fig. 6D and E).

Quantitative assessments were performed to determine the AEPI concentrations in the brain and serum. A standard curve for the AEPI solutions was constructed (Fig. S2). Serum samples were collected at 1 h, and brain tissues were subsequently extracted. The drug concentration of the AEPI-RVG-liposome group in the brain (1334 ± 31.92 ng/g) was always higher than that of the APEI group (48.76 ± 33.02 ng/g). Furthermore, the RVG29 modification increased the AEPI concentration in the brain. Besides, the drug concentration of the AEPI-RVG-liposome group in the serum (11248 ± 672 ng/ml) was significantly higher than that in the APEI group (2733 ± 1675 ng/ml), indicating faster systemic absorption of AEPI-RVG-liposomes following nasal administration compared to the AEPI solution (Table 2).

Overall, these findings demonstrate that RVG29-AEPI liposomes may improve the permeability of therapeutic drugs and overcome BBB challenges when administered via the nasal route.

3.4. RVG29-AEPI liposomes are highly systemically safe

For assessing the biosafety of liposome administration, eight healthy C57BL/6 mice were used. RVG29-AEPI liposomes or PBS were administered intranasally to the mice daily for 14 days.

The histopathology of the organs (heart, liver, spleen, lungs, and kidneys) and blood tests on tissues obtained from each group on day 14 post-irradiation were used to measure *in vivo* toxicity. There were no evident pathological differences between the groups (Fig. 7A), and blood biochemical markers, such as alanine transaminase (ALT), aspartate transaminase (AST), albumin (ALB), and blood urea nitrogen (BUN) in each group were within normal limits (Fig. 7B and C). These findings demonstrate that the RVG29-AEPI liposomes are biosafe and biocompatible.

3.5. RVG29-AEPI liposomes provided excellent radioprotection to the brain

Improving the loss of neurological function induced by radiation is clinically significant. We performed fluorescence and behavioral tests to assess the efficiency of RVG29-AEPI liposomes in preventing RIBI 14 days after irradiation (Fig. 8A).

Every three days, the mice received intranasal delivery of RVG29-

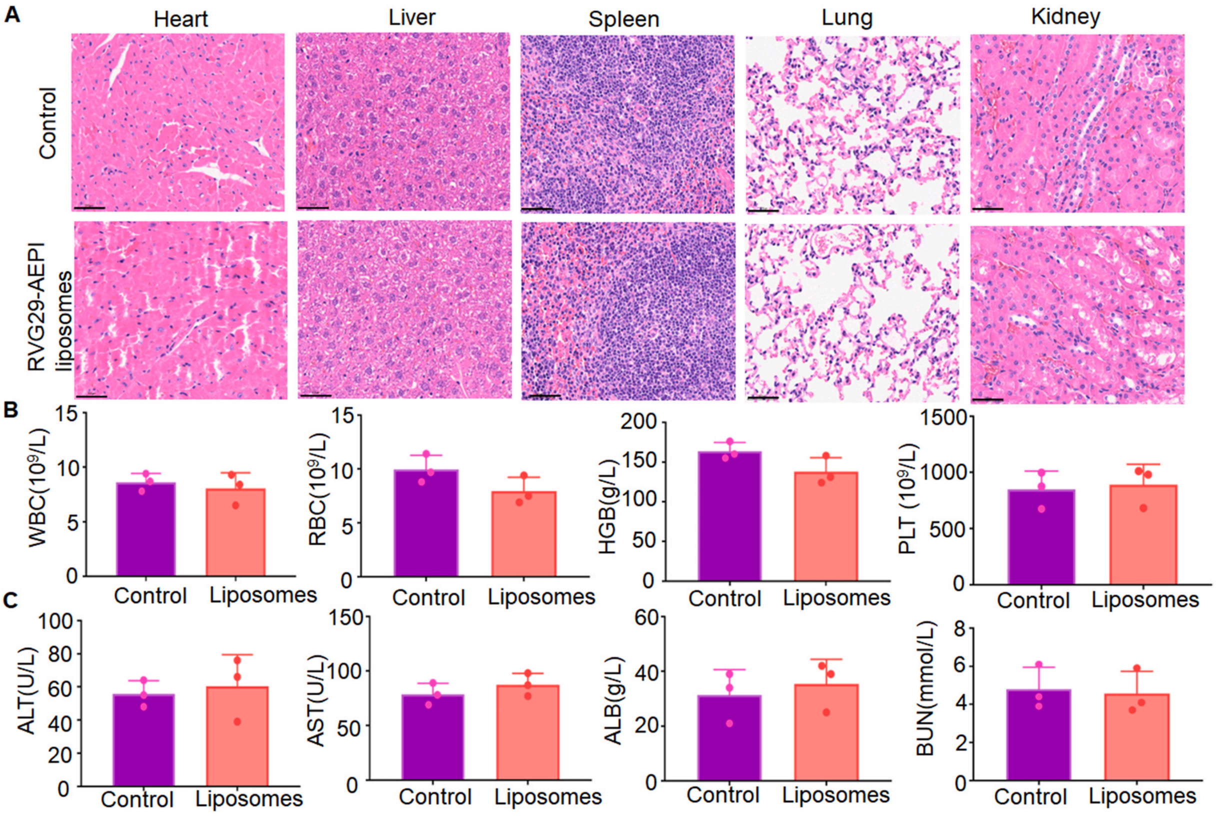

Fig. 7. RVG29-AEPI Liposomes' systemic biosafety *in vivo*. (A) H&E staining slices of major organs taken 14 days after intranasal administration, including the heart, liver, spleen, lung, and kidney. Scale bar: 100 μm. (B, C) Hematology and serum biochemical analysis of mice after 14 days following intranasal administration. The data are shown as the mean ± standard deviation from three separate studies.

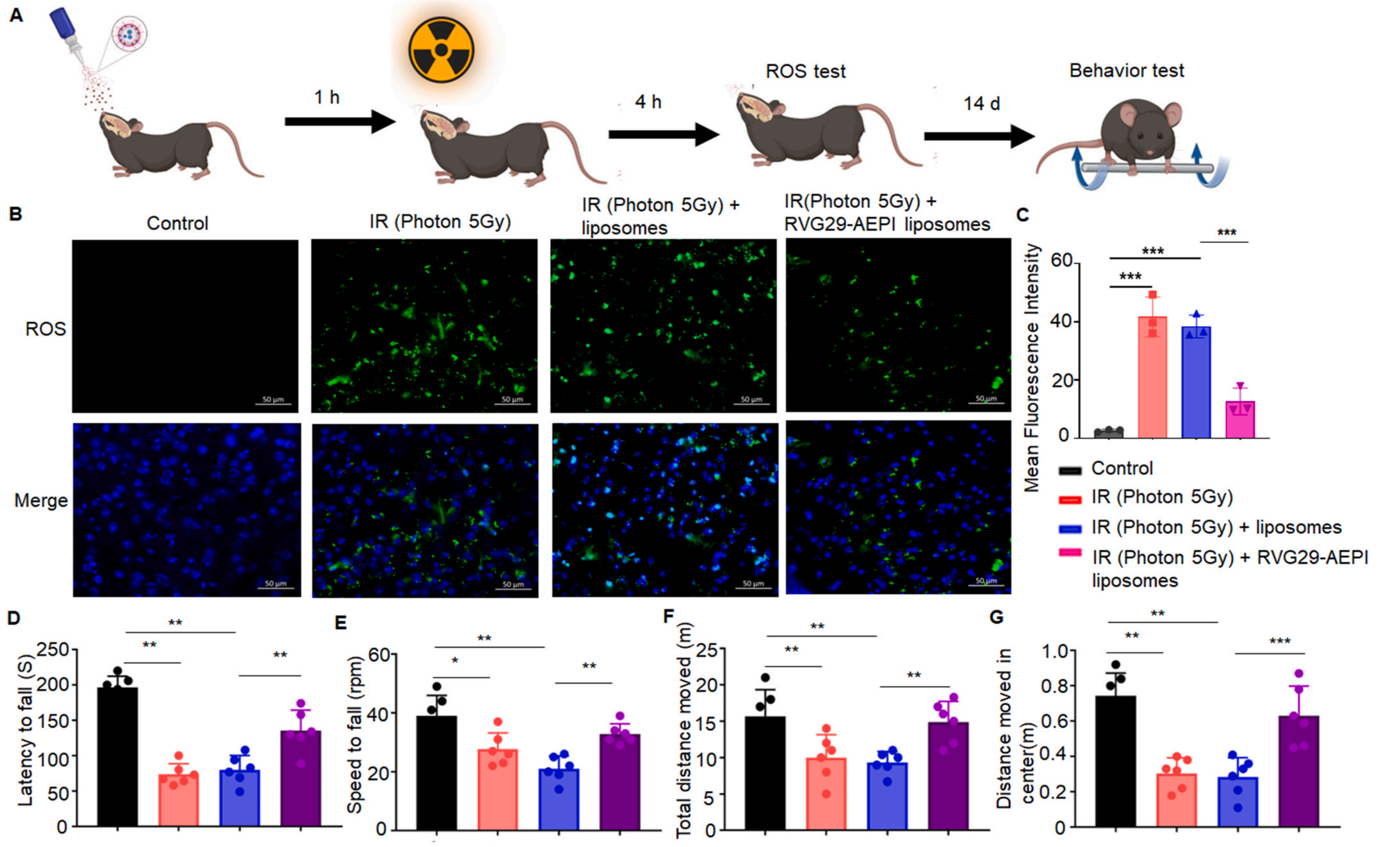

Fig. 8. RVG29-AEPI Liposomes suppress ROS production and exert radioprotection of locomotor activity in rodents under photon therapy. (A) Schematic drawing of the experimental design timeline. (B, C) Fluorescence images for detecting tissue ROS (green signal) produced by the mice's right thalamus following various treatments. Scale bar: 50 μm. (D) Rotarod experiments measuring the latency of mice falling from the rod, with n = 6 per group. (E) Rotarod tests measuring the rod's speed as mice fall, with n = 6 per group. (F) Open field tests measuring the total distance traveled throughout the entire field for several groups (n = 6 each group). (G) Open field tests measuring the distance traveled in the center are conducted across various groups, with n = 6 per group. ***: $p < 0.001$. **: $p < 0.01$. *: $p < 0.05$.

AEPI liposomes, liposomes, or PBS. When the irradiated mice were administered RVG29-AEPI liposomes, the ROS fluorescence signals in right thalamus were much lower than those in the IR + PBS group (Fig. 8B and C). Furthermore, a rotarod performance test was used to evaluate motor coordination in rodents. As expected, the RVG29-AEPI liposome-treated mice maintained a tendency of more time than IR and IR + liposomes groups (Fig. 8D and E). The open field test assessed general locomotor activity levels, anxiety, and willingness to explore, the whole-brain irradiation reduced the total distance moved in the field and in the center, whereas RVG29-AEPI liposome-treated mice presented more activities in the center in comparison with IR or IR + liposomes group (Fig. 8F and G).

Thus, the RVG29-AEPI liposomes provide much greater protection against RIBI when administered intranasally.

3.6. *RVG29-AEPI liposomes reduced radiation-induced neuronal loss and microglia activation under proton and photon irradiation*

The proton beam, characterized by its optimal dose distribution known as the "Bragg peak," is widely used in the treatment of several tumors patients. The role of RVG29-AEPI liposomes in both photon and proton irradiation of neurons and microglial cells was investigated.

NeuN was used to count the number of neurons in the lesions in the cornu ammonis (CA) and gyrus dentatus (GD) areas of the hippocampus and thalamus in photon-irradiated animals (Fig. S3). As expected, the RVG29-AEPI group showed a higher proportion of NeuN-positive cells than IR and IR + liposomes (Figs. S3A–S3D). IBA1 and GFAP were used to detect microglia and astrocytes, respectively. Following photon irradiation, significant activation of microglia and astrocytes was observed in the IR group. Moreover, the RVG29-AEPI liposomes inhibited microglial and astrocytic activation in the right thalamus (Fig. 9 A-9D). As for the new radiotherapy technique, proton therapy with RVG29-AEPI also effectively reduced the activation of microglia and increased the proportion of NeuN + cells after irradiation (Fig. 10A–D). However, no significant difference was observed in the GFAP-positive ratio after proton therapy (Fig. S4).

Taken together, these findings imply that RVG29-AEPI liposomes improve BBB penetration and exert superior protective effects against microglial activation and radiation-induced neuronal death under traditional and novel radiation therapies.

4. Discussion

To reduce the occurrence of RIBI, several novel approaches and strategies have been applied in the field of radiation therapy, including intensity-modulated RT and particle beams with protons, carbon ions, and other heavy ions [21]. However, even when the radiation dose to normal tissues is significantly reduced by proton therapy, RIBI still occurs and remains an obstacle [22]. Clinical studies have shown that glucocorticoids and bevacizumab can be used as first-line treatments, whereas thalidomide and apatinib have successfully completed phase II clinical trials [4,5]. New radiation treatments combined with radioprotectants can be viable conservation strategies. However, therapeutic methods have already been hampered by the paucity of molecular processes involved in RIBI and accurate delivery to crucial brain structures. Interestingly, this study observed that a nose-to-brain conveyance

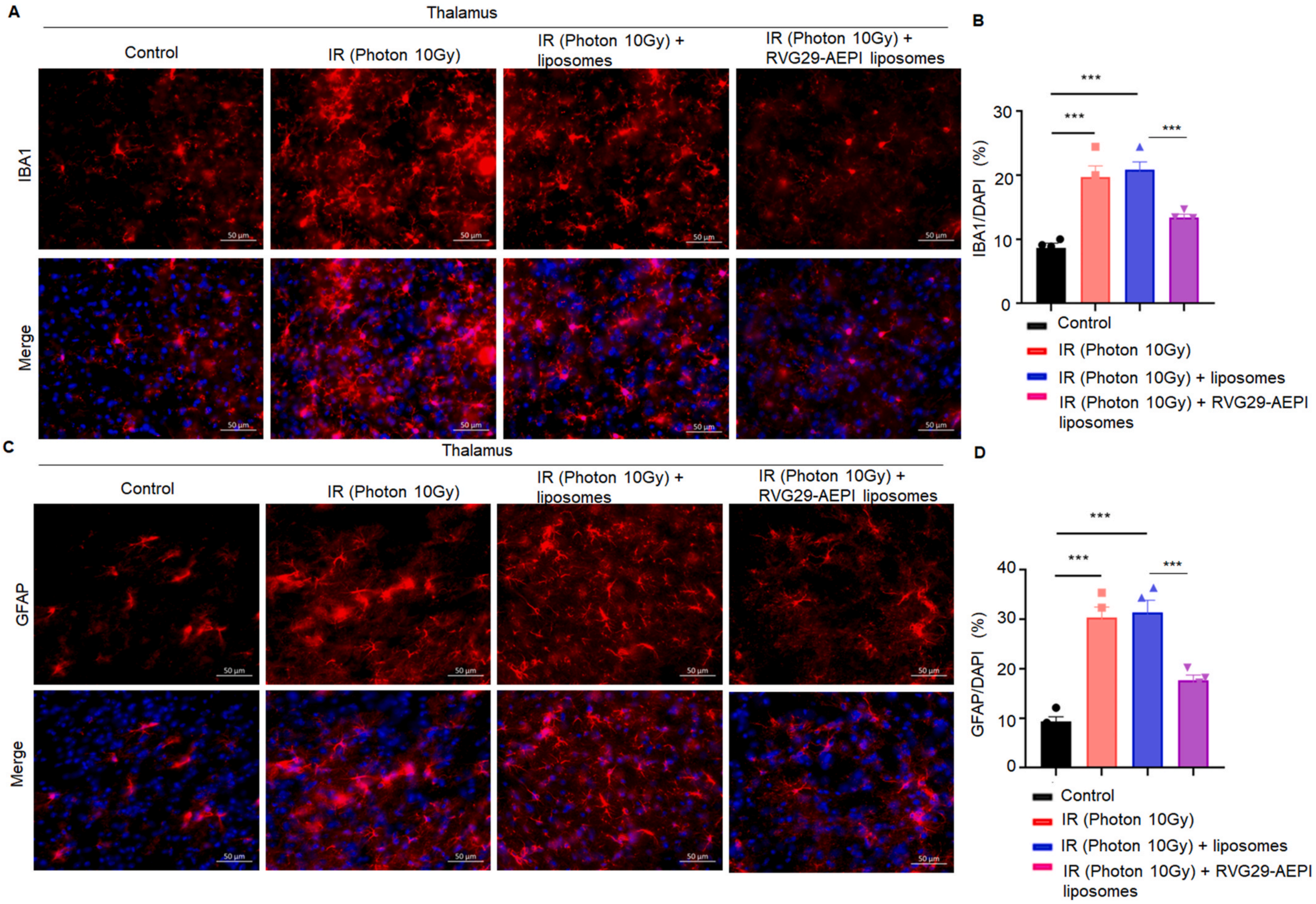

Fig. 9. RVG29-AEPI Liposomes alleviated radiation-induced microglia activation under photon radiation. (A, B) Representative fluorescence images of IBA1 staining in the right thalamus region of mice after different treatments. Scale bar = 50 μm. (C, D) Representative fluorescence images of GFAP staining in the right thalamus region of mice after different treatments. Scale bar = 50 μm ***: $p < 0.001$.

platform for AEPI could achieve these goals simultaneously.

The lysosomal cysteine protease AEP is activated in acidic environments and is linked to the development of certain nervous system disorders. It was recently demonstrated that, following whole-brain irradiation, AEP expression significantly increases in the cortex and hippocampus of WT (Lgmn+/+) mice. On inhibiting neuronal senescence, Lgmn-knockout (Lgmn$^{-/-}$) mice showed reduced neurological damage caused by whole-brain irradiation. This indicates that AEP plays a crucial role in RIBI by modulating neuronal senescence [8]. However, the low blood-brain barrier penetration of AEP-related medications prompted this study. This study described an efficient nose-to-brain administration mechanism for RVG29-AEPI liposomes across the BBB. The liposomes were shown to be more effective in removing ROS and providing cerebral protection.

The morphology of microglia changes significantly after radiation, including enlargement of the cell body, shortening of protrusions, and increased phagocytic activity, all of which contribute to the pathogenesis of RIBI [23]. In addition to structural alterations, mitochondrial respiration is improved in microglia, resulting in increased ROS generation [24]. Excessive ROS causes structural damage to adjacent tissues and serves as secondary messengers, promoting microglial activation. Activated microglia can also release several inflammatory mediators, such as CCL2 and CCL8, to attract the central infiltration of peripheral CD8+T cells and damaged neurons [25]. Moreover, nuclear translocation and release of HMGB1 in injured neurons can promote microglial activation, producing inflammatory substances [26]. Because protease inhibitors have a broad spectrum of activity and their cutting sites are highly preserved, they have an excellent market future. Wang et al. reported that depletion of AEP strongly reduces ROS and neuro-inflammation in α-SNCA mice. AEP cleaved human α-Syn at N103, enhancing its aggregation and toxicity and inducing dopaminergic (DA) neuronal loss and motor disorders [27]. Notably, AEP is upregulated by oxidative stress and implicated in inflammatory responses [28]. Therefore, the effect of AEPI in a murine RIBI model was investigated. Functional experiments were conducted to verify whether AEP treatments could scavenge ROS and alleviate irradiation-induced DNA damage. After irradiation, activation of microglia and astrocytes in the right thalamus was significantly reduced in the RVG29-AEPI liposome-treated group. Unexpectedly, the number of GFAP-positive cells changed slightly under proton irradiation. GFAP, a brain injury marker, demonstrates the biological superiority of proton therapy and can protect normal tissues. Thus, the application of RVG29-AEPI liposomes can suppress microglial activation and protect against brain damage caused by proton irradiation.

The current study has some limitations. Firstly, the precise mechanism underlying AEP cleavage remains unknown and requires further investigation. This substrate may be cleaved by AEP to regulate the RIBI activity. Second, as fractionated radiation in humans more closely resembles clinical radiation scenarios compared to single-dose radiation, which differs from single-dose radiation, future research should focus on developing a specialized mouse model of RIBI to better replicate these conditions.

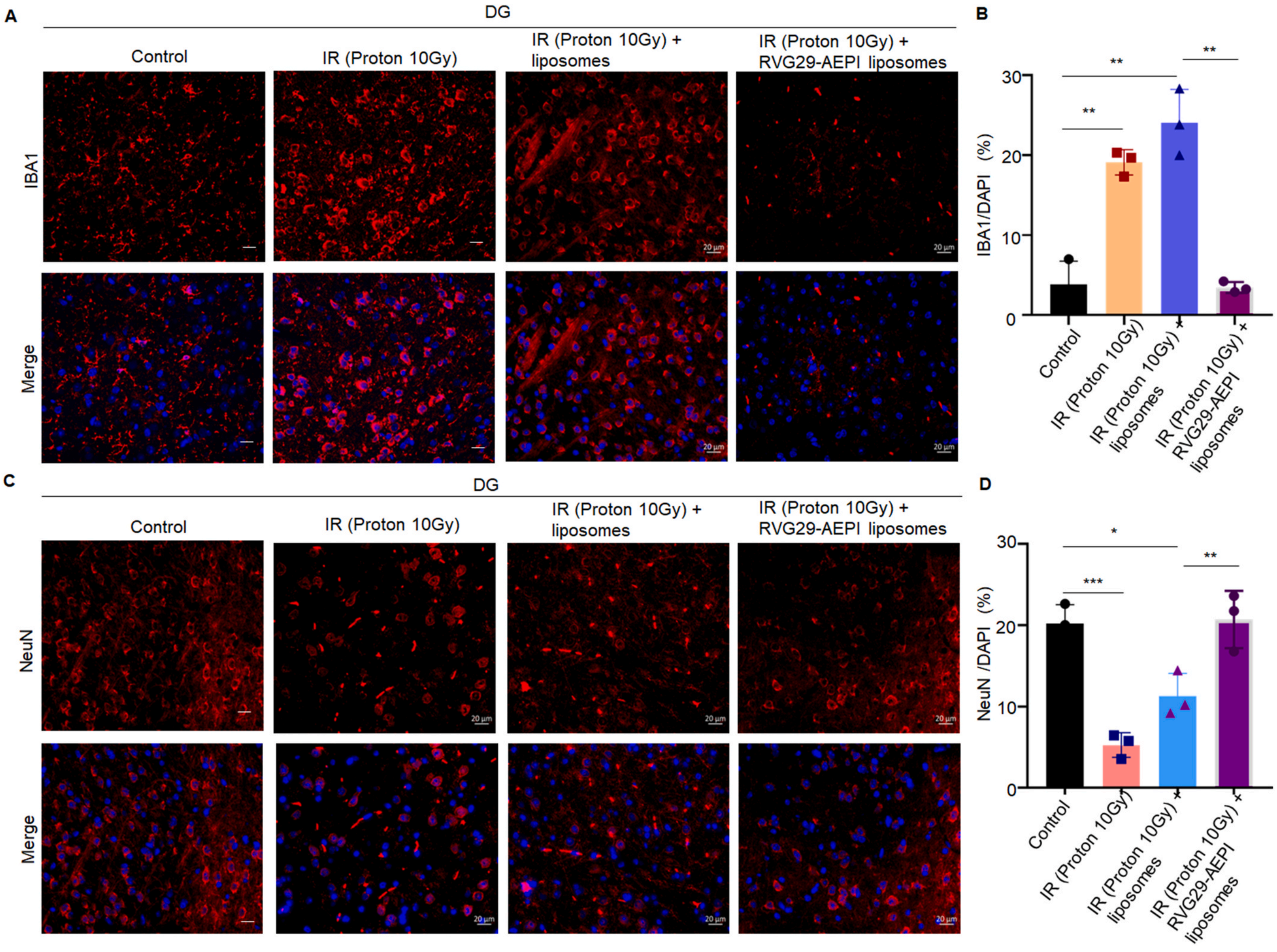

Fig. 10. RVG29-AEPI Liposomes alleviated radiation-induced microglia activation under proton therapy. (A, B) Representative fluorescence images of IBA1 staining in the DG region of mice after different treatments under proton therapy. Scale bar = 20 μm. (C, D) Representative fluorescence images of NeuN staining in the DG of mice after different treatments under proton therapy. Scale bar = 20 μm ***: $p < 0.001$, **: $p < 0.01$, *: $p < 0.05$.

5. Conclusion

This study effectively created a reliable nose-to-brain AEPI delivery system. The combination of RVG29-AEPI liposomes effectively passed through the BBB and significantly reduced radiation-induced neuronal damage, microglial activation, and brain injury *in vivo*. Adequate radioprotection can be provided using customized liposomes to transfer AEPI from the nose to the brain, thus expediting the therapeutic process.

CRediT authorship contribution statement

Keman Liao: Writing – original draft, Validation, Methodology, Investigation, Funding acquisition, Formal analysis, Data curation, Conceptualization. **Yan Gao:** Writing – original draft, Validation, Methodology, Investigation, Formal analysis, Data curation, Conceptualization. **Mengdan Cheng:** Writing – original draft, Validation, Methodology, Investigation, Formal analysis, Data curation, Conceptualization. **Yibing Zhang:** Writing – original draft, Validation, Investigation, Formal analysis, Data curation, Conceptualization. **Jianyi Zhao:** Writing – original draft, Investigation, Formal analysis. **Li Zhou:** Methodology, Data curation. **Ran Wu:** Validation, Formal analysis. **Gang Cai:** Writing – original draft, Visualization, Validation, Supervision, Investigation, Formal analysis. **Lu Cao:** Writing – original draft, Visualization, Supervision, Methodology, Investigation, Formal analysis, Data curation, Conceptualization. **Jiayi Chen:** Visualization, Validation, Supervision, Methodology, Investigation, Funding acquisition, Formal analysis, Data curation, Conceptualization. **Yingying Lin:** Writing – original draft, Visualization, Validation, Supervision, Resources, Project administration, Methodology, Investigation, Funding acquisition, Formal analysis, Data curation, Conceptualization.

Funding

This work was supported by the National Key R&D Program of China (grant number 2023ZD0502206), National Natural Science Foundation of China (nos. 81772654, 82373514, 82002630) and China Postdoctoral Science Foundation (nos. 2024M752028), Shanghai Association for Science and Technology (nos. 201409003000), Shanghai Science and Technology Innovation Action Plan (grant number 23Y41900100), the National Key Research and Development Program of China (grant number 2022YFC2404602), Shanghai Hospital Development Center Foundation (grant number SHDC12023108), Scientific and Technological Innovation Action Plan of Shanghai Science and Technology Committee (grant number 22Y31900103), Beijing Science and Technology Innovation Medical Development Foundation (grant number KC2021-JX-0170-9).

Declaration of competing interest

The authors declare that they have no known competing financial interests or personal relationships that could have appeared to influence the work reported in this paper.

Acknowledgements

Sample processing was conducted in Jiangnan University Medical Center.

Appendix A. Supplementary data

Supplementary data to this article can be found online at https://doi.org/10.1016/j.mtbio.2025.101568.

Data availability

Data will be made available on request.

References

[1] F.S. Ali, O. Arevalo, S. Zorofchian, A. Patrizz, R. Riascos, N. Tandon, A. Blanco, L. Y. Ballester, Y. Esquenazi, Cerebral radiation necrosis: incidence, pathogenesis, diagnostic challenges, and future opportunities, Curr. Oncol. Rep. 21 (2019) 66, https://doi.org/10.1007/s11912-019-0818-y.

[2] M. Nakamura, T. Yamasaki, M. Ueno, S. Shibata, Y. Ozawa, T. Kamada, I. Nakanishi, K.I. Yamada, I. Aoki, K.I. Matsumoto, Radiation-induced redox alteration in the mouse brain, Free Radic. Biol. Med. 143 (2019) 412–421, https://doi.org/10.1016/j.freeradbiomed.2019.08.020.

[3] C. Lutgendorf-Caucig, M. Pelak, E. Hug, B. Flechl, B. Surbock, C. Marosi, U. Mock, L. Zach, Y. Mardor, O. Furman, et al., Prospective analysis of radiation-induced contrast enhancement and health-related quality of life after proton therapy for central nervous system and skull base tumors, Int. J. Radiat. Oncol. Biol. Phys. 118 (2024) 1206–1216, https://doi.org/10.1016/j.ijrobp.2024.01.007.

[4] L. He, Y. Pi, Y. Li, Y. Wu, J. Jiang, X. Rong, J. Cai, Z. Yue, J. Cheng, H. Li, M.L. K. Chua, Simone CB 2nd, W.S. Aronow, S. Lattanzi, J.D. Palmer, J. Gaertner, J. Glass, P. Chen, Y. Tang, Efficacy and safety of apatinib for radiation-induced brain injury among patients with head and neck cancer: an open-label, single-arm, phase 2 study, Int. J. Radiat. Oncol. Biol. Phys. 113 (4) (2022 Jul 15) 796–804, https://doi.org/10.1016/j.ijrobp.2022.03.027.

[5] J. Cheng, J. Jiang, B. He, W.J. Lin, Y. Li, J. Duan, H. Li, X. Huang, J. Cai, J. Xie, Z. Zhang, Y. Yang, Y. Xu, X. Hu, M. Wu, X. Zhuo, Q. Liu, Z. Shi, P. Yu, X. Rong, X. Ye, P.E. Saw, L.J. Wu, C.B. Simone 2nd, M.L.K. Chua, H.Q. Mai, Y. Tang, A phase 2 study of thalidomide for the treatment of radiation-induced blood-brain barrier injury, Sci. Transl. Med. 15 (684) (2023 Feb 22) eabm6543, https://doi.org/10.1126/scitranslmed.abm6543.

[6] S. Derby, M.R. Jackson, K. Williams, J. Stobo, C. Kelly, L. Sweeting, S. Shad, C. Herbert, S.C. Short, A. Williamson, A. James, S. Nowicki, H. Bulbeck, A. J. Chalmers, Concurrent olaparib and radiation therapy in older patients with newly diagnosed glioblastoma: the phase 1 dose-escalation PARADIGM trial, Int. J. Radiat. Oncol. Biol. Phys. 118 (5) (2024 Apr 1) 1371–1378, https://doi.org/10.1016/j.ijrobp.2024.01.011.

[7] C. Chu, Y. Gao, X. Lan, J. Lin, A.M. Thomas, S. Li, Stem-cell therapy as a potential strategy for radiation-induced brain injury, Stem Cell Rev Rep 16 (4) (2020 Aug) 639–649, https://doi.org/10.1007/s12015-020-09984-7.

[8] [8]a H. Zhou, F. Sun, M. Ou, Y. Zhang, M. Lin, L. Song, Y. Yu, H. Liao, W. Fan, H. Xing, M. Li, K. Zhao, X. Wu, Y. Sun, C. Liang, Y. Cai, L. Cui, Prior nasal delivery of antagomiR-122 prevents radiation-induced brain injury, Mol. Ther. 29 (12) (2021 Dec 1) 3465–3483, https://doi.org/10.1016/j.ymthe.2021.06.019;
[8]b O. Qiu, J. Zhao, Z. Shi, H. Li, S. Wang, K. Liao, M. Tang, J. Xie, X. Huang, W. Zhang, et al., Asparagine endopeptidase deficiency mitigates radiation-induced brain injury by suppressing microglia-mediated neuronal senescence, iScience 27 (2024) 109698, https://doi.org/10.1016/j.isci.2024.109698.

[9] Z. Qian, B. Li, X. Meng, J. Liao, G. Wang, Y. Li, Q. Luo, K. Ye, Inhibition of asparagine endopeptidase (AEP) effectively treats sporadic Alzheimer's disease in mice, Neuropsychopharmacology 49 (2024) 620–630, https://doi.org/10.1038/s41386-023-01774-2.

[10] D. Krummenacher, W. He, B. Kuhn, C. Schnider, A. Beurier, V. Brom, T. Sivasothy, C. Marty, A. Tosstorff, D.S. Hewings, et al., Discovery of orally available and brain penetrant AEP inhibitors, J. Med. Chem. 66 (2023) 17026–17043, https://doi.org/10.1021/acs.jmedchem.3c01804.

[11] Z. Wu, R. Zhu, Y. Yu, J. Wang, X. Hu, W. Xu, Y. Ren, C. Li, Z. Zeng, B. Ma, et al., Spinal cord injury-activated C/EBPbeta-AEP axis mediates cognitive impairment through APP C586/Tau N368 fragments spreading, Prog Neurobiol 227 (2023) 102467, https://doi.org/10.1016/j.pneurobio.2023.102467.

[12] Y. Lin, K. Liao, Y. Miao, Z. Qian, Z. Fang, X. Yang, Q. Nie, G. Jiang, J. Liu, Y. Yu, et al., Role of asparagine endopeptidase in mediating wild-type p53 inactivation of glioblastoma, J Natl Cancer Inst (2019), https://doi.org/10.1093/jnci/djz155.

[13] B. Chen, M. Wang, J. Qiu, K. Liao, W. Zhang, Q. Lv, C. Ma, Z. Qian, Z. Shi, R. Liang, et al., Cleavage of tropomodulin-3 by asparagine endopeptidase promotes cancer malignancy by actin remodeling and SND1/RhoA signaling, J. Exp. Clin. Cancer Res. 41 (2022) 209, https://doi.org/10.1186/s13046-022-02411-4.

[14] W. Zhang, L. Cao, J. Yang, S. Zhang, J. Zhao, Z. Shi, K. Liao, H. Wang, B. Chen, Z. Qian, et al., AEP-cleaved DDX3X induces alternative RNA splicing events to mediate cancer cell adaptation in harsh microenvironments, J. Clin. Investig. 134 (2023), https://doi.org/10.1172/JCI173299.

[15] J.A. Miranda, Y.F.D. Cruz, I.C. Girao, F.J.J. Souza, W.N. Oliveira, E.D.N. Alencar, L. Amaral-Machado, E. Egito, Beyond traditional sunscreens: a review of liposomal-based systems for photoprotection, Pharmaceutics 16 (2024), https://doi.org/10.3390/pharmaceutics16050661.

[16] M. Sela, M. Poley, P. Mora-Raimundo, S. Kagan, A. Avital, M. Kaduri, G. Chen, O. Adir, A. Rozencweig, Y. Weiss, et al., Brain-targeted liposomes loaded with monoclonal antibodies reduce alpha-synuclein aggregation and improve behavioral symptoms in Parkinson's disease, Adv Mater 35 (2023) e2304654, https://doi.org/10.1002/adma.202304654.

[17] Z. Zhang, W. Cao, H. Xing, S. Guo, L. Huang, L. Wang, X. Sui, K. Lu, Y. Luo, Y. Wang, et al., A mix & act liposomes of phospholipase A2-phosphatidylserine for acute brain detoxification by blood−brain barrier selective-opening, Acta Pharm. Sin. B 14 (2024) 1827–1844, https://doi.org/10.1016/j.apsb.2023.11.015.

[18] Y. Li, Z. Zhang, J. Huang, H. Xing, L. Wang, L. Huang, X. Sui, Y. Luo, L. Shen, Y. Wang, et al., A fast-acting brain-targeted nano-delivery system with ultra-simple structure for brain emergency poisoning rescue, Nanoscale 15 (2023) 4852–4862, https://doi.org/10.1039/d2nr05093e.

[19] W. Zhang, H. Chen, L. Ding, J. Gong, M. Zhang, W. Guo, P. Xu, S. Li, Y. Zhang, Trojan horse delivery of 4,4'-dimethoxychalcone for parkinsonian neuroprotection, Adv. Sci. 8 (9) (2021 Mar 3) 2004555, https://doi.org/10.1002/advs.202004555.

[20] T.L. Lentz, T.G. Burrage, A.L. Smith, J. Crick, G.H. Tignor, Is the acetylcholine receptor a rabies virus receptor? Science 215 (4529) (1982 Jan 8) 182–184, https://doi.org/10.1126/science.7053569.

[21] R.A. Chandra, F.K. Keane, F.E.M. Voncken, C.R. Thomas Jr., Contemporary radiotherapy: present and future, Lancet 398 (10295) (2021 Jul 10) 171–184, https://doi.org/10.1016/S0140-6736(21)00233-6.

[22] C. Betlazar, R.J. Middleton, R.B. Banati, G.J. Liu, The impact of high and low dose ionising radiation on the central nervous system, Redox Biol. 9 (2016) 144–156, https://doi.org/10.1016/j.redox.2016.08.002.

[23] Q. Liu, Y. Huang, M. Duan, Q. Yang, B. Ren, F. Tang, Microglia as therapeutic target for radiation-induced brain injury, Int. J. Mol. Sci. 23 (15) (2022 Jul 27) 8286, https://doi.org/10.3390/ijms23158286.

[24] J.S. Stoolman, R.A. Grant, T.A. Poor, S.E. Weinberg, K.B. D'Alessandro, J. Tan, J. Y. Hu, M.E. Zerrer, W.A. Wood, M.C. Harding, S. Soni, K.M. Ridge, P. T. Schumacker, G.R.S. Budinger, N.S. Chandel, Mitochondrial respiration in microglia is essential for response to demyelinating injury but not proliferation, Nat. Metab. 6 (8) (2024 Aug) 1492–1504, https://doi.org/10.1038/s42255-024-01080-1.

[25] Z. Shi, P. Yu, W.J. Lin, S. Chen, X. Hu, S. Chen, J. Cheng, Q. Liu, Y. Yang, S. Li, Z. Zhang, J. Xie, J. Jiang, B. He, Y. Li, H. Li, Y. Xu, J. Zeng, J. Huang, J. Mei, J. Cai, J. Chen, L.J. Wu, H. Ko, Y. Tang, Microglia drive transient insult-induced brain injury by chemotactic recruitment of CD8$^+$ T lymphocytes, Neuron 111 (5) (2023 Mar 1) 696–710, https://doi.org/10.1016/j.neuron.2022.12.009, e9.

[26] Z. Zhang, J. Jiang, Y. He, J. Cai, J. Xie, M. Wu, M. Xing, Z. Zhang, H. Chang, P. Yu, S. Chen, Y. Yang, Z. Shi, Q. Liu, H. Sun, B. He, J. Zeng, J. Huang, J. Chen, H. Li, Y. Li, W.J. Lin, Y. Tang, Pregabalin mitigates microglial activation and neuronal injury by inhibiting HMGB1 signaling pathway in radiation-induced brain injury, J. Neuroinflammation 19 (1) (2022 Sep 21) 231, https://doi.org/10.1186/s12974-022-02596-7.

[27] E.H. Ahn, S.S. Kang, X. Liu, G. Chen, Z. Zhang, B. Chandrasekharan, A.M. Alam, A. S. Neish, X. Cao, K. Ye, Initiation of Parkinson's disease from gut to brain by δ-secretase, Cell Res. 30 (1) (2020 Jan) 70–87, https://doi.org/10.1038/s41422-019-0241-9.

[28] E.H. Ahn, K. Lei, S.S. Kang, Z.H. Wang, X. Liu, W. Hong, Y.T. Wang, L.E. Edgington-Mitchell, L. Jin, K. Ye, Mitochondrial dysfunction triggers the pathogenesis of Parkinson's disease in neuronal C/EBPβ transgenic mice, Mol Psychiatry 26 (12) (2021 Dec) 7838–7850, https://doi.org/10.1038/s41380-021-01284-x.